Lehrstuhl für Regelungstechnik

Technical Reports on Automatic Control
Vol. TRAC-5, July 21, 2010
Available online at: www.rt.mw.tum.de

TECHNISCHE UNIVERSITÄT MÜNCHEN

Design and Modeling of a Quarter-Vehicle Test Rig for Active Suspension Control

Guido Koch*, Enrico Pellegrini, Sebastian Spirk and Boris Lohmann
Institute of Automatic Control, Technische Universität München
Boltzmannstr. 15, D-85748 Garching, Germany

Abstract

This report presents a quarter-vehicle test rig for an active suspension system that has been designed to study the nonlinear dynamic behavior of suspension systems and to experimentally validate controllers for active suspension systems. A quadricycle suspension system is integrated in the test rig in order to reduce the test rig's mass and to facilitate the realization of a high bandwidth active suspension system. The active suspension is realized by an electrical linear motor which is incorporated in parallel to the passive suspension strut. In the first part of this report, the test rig concept is presented including the actuator and sensor configuration. In the second part, the identification of the test rigs' dynamic behavior is presented and a nonlinear as well as a linear test rig model are derived and validated.

Keywords: Vehicle suspension; Active suspension control; Quarter-vehicle test rig; Identification.

1 Introduction

In the last decade active and semi-active suspension systems for automobiles have gained significant attention. In an active mechatronic suspension system an actuator is integrated in the vehicle suspension to apply forces between chassis and wheel mass independent of the relative motion of these masses [12]. The advantage of such systems over passive suspension systems is their ability to ease the conflict between ride comfort and safety in suspension design: On the one hand, good isolation of the chassis from the road induced vibration is needed whereas on the other hand a stiff, well damped coupling between the wheel and the road surface is necessary to prevent the wheel from lifting from the ground, and thus ensuring the transmission of forces between the tire and the road. A high bandwidth active suspension system (also called fully active suspension) marks the most complex mechatronic suspension that can achieve the best performance in terms of comfort and ride safety enhancement [6, 12]. The bandwidth of fully active suspension systems is approx. 25 Hz in order to damp resonance of the chassis mass (approx. 1 Hz) and the wheel hop mode at approx. 11 Hz.

A research project of the authors deals with active damping in the presence of stochastic disturbances and in particular control concepts for mechatronic suspension systems. In order to study the performance of controllers for high bandwidth active suspensions in a realistic framework,

*Corresponding author: Tel: +49 89 289 15663, Fax: +49 89 289 15653, email: guido.koch@tum.de

a quadricycle is used as an experimental vehicle and half of its front suspension system is integrated in a quarter-vehicle test rig. An actuator is mounted in parallel to the passive suspension system on the test rig to control the motions of the chassis and the wheel mass.

Frequently, linear models are used for the design of suspension controllers. In order to analyze the influence of nonlinearities on the dynamic behavior, identification experiments are conducted at the test rig to determine the main nonlinearities of the suspension components. Especially the nonlinearities of the damper and the tire should be identified as well as relevant friction effects. These informations are used to construct a precise model of the suspension for the synthesis of high performance active suspension controllers and to provide a simulation platform for the controller performance before their implementation at the test rig. Therefore, the model should match the behavior of the system within the control bandwidth ($0 - 25\,\mathrm{Hz}$).

This report is organized as follows: First, the requirements for the test rig are summarized and the quad suspension system is presented in Section 2. In Section 3 the sensors, actuators and digital signal processing hardware used in the test rig are described. Section 4 describes the modeling and identification of the test rig starting with the structure of a quarter-vehicle model. The identification of the actuator dynamics and the nonlinear component characteristics is presented and the optimization based parametrization is described. A performance comparison of the nonlinear model and its linearization is presented in Section 4.6. Finally, a conclusion is given in Section 5.

2 Test rig concept

2.1 Requirements

The requirements of the test rig can be summarized as follows:

- Similar dynamic behavior in terms of nonlinearities, damping and resonance frequencies of chassis and wheel mass as a car suspension [12].
- Ideally frictionless vertical guidance of the chassis mass.
- Possibility to apply realistic excitation signals (amplitudes of up to $5\,\mathrm{cm}$) within the frequency range $0 - 25\,\mathrm{Hz}$.
- Realization of a fully active suspension configuration with an actuator integrated in parallel to the suspension strut and a control bandwidth of at least $25\,\mathrm{Hz}$.

2.2 Quad suspension

A quadricycle/all-terrain-vehicle has been chosen as experimental vehicle due to its lower masses compared to an automobile but its comparable suspension configuration. The suspension system (Figure 1) basically consists of the tire, the double wishbone struts connected via two ball-joints to the wheel carrier and the suspension strut with the primary spring and the damper. The suspension strut is linked between the lower wishbone strut and the chassis via slide bearings. The spring and the damper are slightly inclined in the equilibrium position. Unlike a McPherson suspension, the suspension strut at hand does not have a guiding function for the wheel.

The suspension kinematics determined by the double wishbone configuration and the steering track rod result in camber and toe-in changes during compression and rebound of the spring. On the wheel carrier the disc-brake is attached and the wheel is mounted on it. The wheel consists of an aluminium rim with a tire featuring a road pattern.

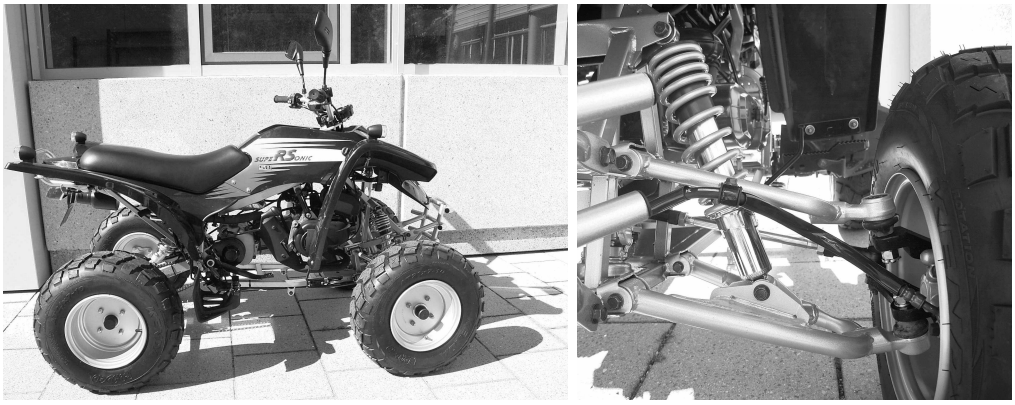

Figure 1: Experimental quadricycle vehicle (left), left front suspension (right)

The smaller sprung and unsprung masses of the quadricycle suspension correspond to smaller stiffnesses and damping ratio compared to a car but its damping-isolation behavior is similar compared to an automobile suspension system. The main differences can be summarized to:

- Lower masses, primary spring and tire stiffness (tire air-pressure approx. 1.4 bar compared to approx. 2.2 bar), respectively.
- No rubber-mounts are integrated for the mounting of the double wishbones to the chassis. These are used in cars in order to enhance the performance of the vehicle suspension regarding acoustics and vibration-isolation [12]. In the quad suspension, stiff slide bearings are integrated and therefore no elasto-kinematic effects are present at the wishbone strut attachments.

3 Realization of the quarter-vehicle test rig

The test rig has first been realized for the passive suspension (Figure 2 lower left) and has then been upgraded to realize the high bandwidth active suspension (Figure 2 lower right). The test rig incorporates the left front suspension shown in Figure 1, which is mounted on a vertically guided steel plate at the double wishbone struts and the primary spring. The steel plate has a mass of 29 kg and symbolizes in combination with the components attached to it, approximately a quarter of the vehicle mass including driver, i.e. approx. 60 kg for the passive setting and 90 kg for the active suspension. The plate is guided vertically by steel rolls on roller bearings. Due to remaining static and dynamic friction effects, low friction forces proportional to the absolute velocity of the chassis mass occur, which are, however, less distinct in the suspension assembly of the real vehicle and need to be considered in the test rig model (see Section 4.3.3).

Although no external steering command is applied to the wheel of the test rig, the steering bar is integrated on the test-rig in order to appropriately simulate the kinematics of the wheel during the compression cycle of the suspension strut. If the suspension strut is compressed, the wheel track changes due to the steering track rod. Because the wheel cannot perform roll motions, its base plate is guided horizontally to reduce translational forces on the base plate below the wheel. Due to the toe-in changes during spring compression and rebound, the wheel rests on a mounted disc with a rotatory degree of freedom in order to also reduce the transmission of friction torques to the base plate.

The tire is excited by an electrical linear motor that emulates the road induced vibrations. In order to compensate the gravitational force of the moving parts of the test rig, the static load is

supported by four springs. The springs influence the excitation signals only marginally because the actuator position is controlled. In order to take the remaining alteration of the excitation signals into account, the movement of the wheel base plate (excitation signal) is measured by an incremental encoder of the linear motor. Hence, the measured signal can be used as disturbance input in simulations in order to ensure comparability of measurement and simulation results. The rod of the actuator is mounted to the base plate and is guided by an axial roller bearing in order to avoid lateral forces and torques on the actuator rod.

For the realization of the active suspension system, a second electrical linear motor is integrated between the tire and the wheel. Its rod is attached to the wheel carrier. In order to compensate for the additional unsprung mass of the rod, the original steel rim of the vehicle have been replaced by an aluminium light alloy rim.

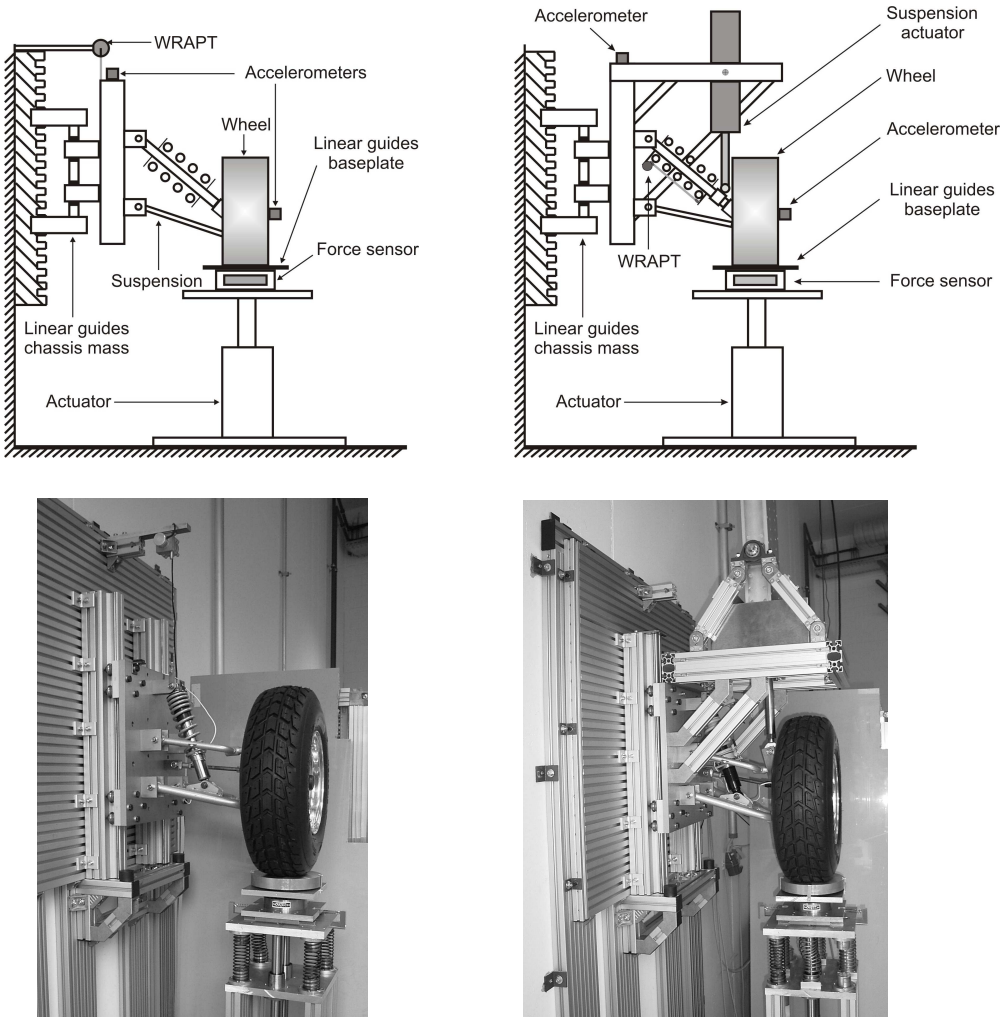

Figure 2: Test rig concepts and corresponding realizations for passive (le.) and active (ri.) suspension settings

3.1 Sensors

The measurement signals and integrated sensors of the test rig are:

- Chassis acceleration: $\ddot{x}_c$ measured by a capacitive accelerometer,
- Suspension deflection: $x_c - x_w$, recorded by a wire rope actuated position transducer (WRAPT),
- Wheel acceleration: $\ddot{x}_w$, measured by a capacitive accelerometer,
- Wheel load: F_w, measured by resistance strain gauge based force sensor,
- Wheel position: x_g measured by an incremental encoder,
- Upper actuator current: $i_q(t)$ measured by the actuator's inverter.

In the test rig two accelerometers are used, in order to capture the acceleration of the chassis and the wheel mass. For the chassis mass acceleration, a sensor with a measurement range of ±5g is used and for the wheel acceleration ±25g, respectively. The accelerometers are capacitive sensors and combine components with high drive, low impedance buffering for measuring acceleration that allow a good sensitivity in the low frequency range. The anodized aluminum case is epoxy sealed. An on-board regulation is provided to minimize the effects of supply voltage variation. Every sensor produces two analog voltage outputs which vary with acceleration. The signal outputs are fully differential with respect to a common mode voltage of approximately 2.5 V. At zero acceleration the output differential voltage is nominally 0 V DC, at full scale acceleration the output differential voltage is ±4 V DC, respectively. The relevant technical data are summarized in Table 1.

Table 1: Accelerometer specifications

Analog Accelerometer Module		
	Chassis	Wheel
Max. operating frequency range	400 Hz	1000 Hz
Measurement range	$\pm 5g$	$\pm 25g$
Input voltage	9...32V DC	9...32V DC
Voltage supply	15 V± 2 mV	15 V± 2 mV
Differential measurement signal	800mV/g	160mV/g
Noise (rms)	32μg	158μg
Offset deviation	3% of measurement range	3% of measurement range
Max. absolute deviation	0.75g	0.75g
Max. relative deviation	1%	1%

On the test rig a strain gauge based load cell placed below the wheel is used to measure the wheel load. This type of load cell is designed for high levels of cycling loads. The load cell has accurate output symmetry between compression and tension operation. The technical specifications are summarized in Table 2. The sensor output is amplified by a standard strain gauge amplifier.

For the measurement of the suspension deflection a wire rope actuated position transducer (WRAPT) with a digital incremental encoder is used. The sensor is installed parallel[1] to the suspension strut (see Figure 2) and delivers a relative signal with a resolution of 12 pulses per mm in a maximum measurement range of 1250 mm. Its linear deviation within the measurement range is below 0.05%.

[1] Only for friction measurements, the sensor is mounted above the chassis mass (see Section 4.3.3)

Table 2: Load cell specifications

Strain gauge force sensor	
DMS-feed	10 V_{DC}
Operating voltage	$\pm 15 V_{DC}$ (controlled)
Operating range	0... $\pm$ 10V
Sensitivity	2mV/V $\pm$0.5%
Amplifier analog output	0... $\pm$ 10V
Cutoff frequency (-3dB)	1kHz

3.2 Actuators

3.2.1 Excitation Actuator For the vertical excitation of the wheel an electrical linear motor (Figure 3) is connected to the wheel's base plate. According to the principle of a brushless three-phase electro motor a force is generated directly proportional to the current moving the rod, which incorporates the permanent magnets.

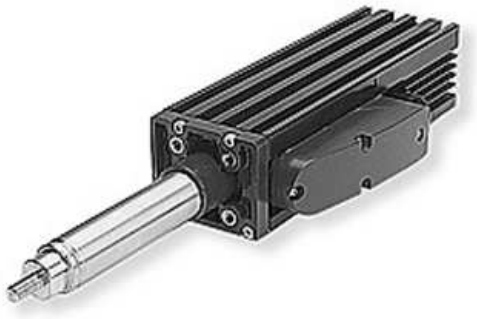

Figure 3: Linear motor for the road excitation

The linear motor can generate high peak forces of up to 1860 N but the maximum peak force is limited to 1 sec and the force rms-value[2] may not exceed 276 N. Therefore, the actuator is used only for the dynamical excitation and the static load of the test rig is carried by a parallel connection of four springs. The displacement of the actuator is measured. An algorithm of the control software compares the actual current with the continuously allowed current value and integrates the difference. If the value I^2T_{acc} (accumulated I^2T) exceeds the maximal operating time in the overload range I^2T_{set} (I^2T setpoint), the current will be limited to the continuously allowed value until the integrator value has reduced. The parameters are calculated using the output current $i_{out}(t)$, the continuous current limit $\|i\|_{\text{rms},lim}$ and the peak current limit $\hat{i}_{lim}$ as follows

$$\begin{aligned} I^2T_{acc} &= \int i_{out}^2(t) - \|i\|_{\text{rms},lim}^2 dt, \\ I^2T_{set} &= (\hat{i}_{lim}^2 - \|i\|_{\text{rms},lim}^2) \cdot 1\,\text{sec}. \end{aligned} \tag{1}$$

The actuator is driven by an inverter and amplifier. By regulating the actuator current, which is proportionally related to the force, the amplifier controls velocity and position of the motor

[2]The rms-value of a signal $x(t)$ is defined as $\|x(t)\|_{\text{rms}} = \sqrt{\frac{1}{T}\int_0^T x^2(t)\ dt}$.

rod. The control software has a cascade control structure using the digital motor position, its derivate and current feedback to ensure the rod position following the analog command input.

The commanded position is manipulated by a dead zone around the idle state to avoid dithering due to a noisy input signal. The position command and the resulting profile velocity and acceleration are limited (Figure 4). Velocity and acceleration are used for feedforward control of the velocity loop shown in Figure 5. The position deviation is multiplied by a feedback gain and added to the desired velocity value. The desired velocity is controlled by the PI feedback control shown in Figure 6 that drives the current setpoint. Two filters reduce noise effects and the velocity limits are monitored. The current is also controlled by a PI feedback loop (Figure 7), furthermore an offset can be added to the desired force value for static loads, which are small in the case at hand due to the base plate springs.

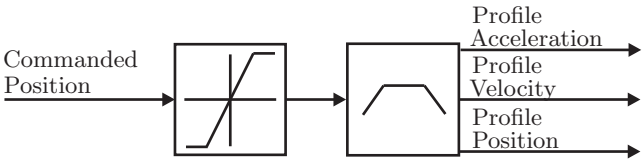

Figure 4: Position command derivation and limitation

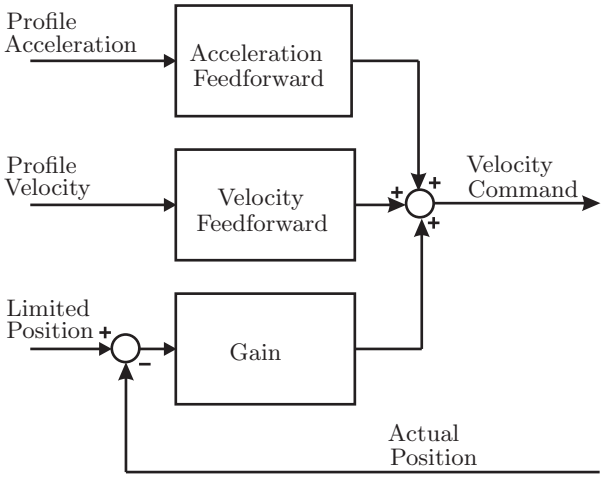

Figure 5: Command feedforward and position feedback control

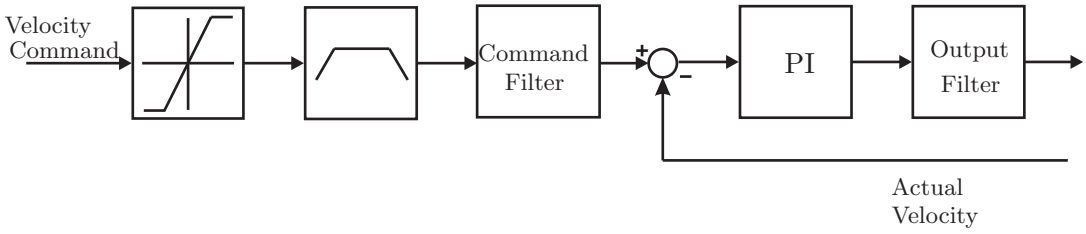

Figure 6: Velocity control loop

3.2.2 Suspension Actuator The linear motor was custom made for the authors' institute by *EAAT GmbH* (Chemnitz). The technical specifications of the flat ironless synchronous, permanent excited, linear motor (see Fig. 8) are summarized in Table 3. Because the actuator is integrated in parallel to the passive suspension strut, its rod should be movable with low

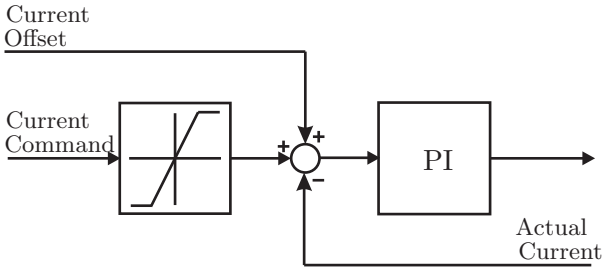

Figure 7: Current loop

friction in order to minimize alteration of the passive suspension's dynamic behavior. The motor model *FL-135 468 SL* has been selected because its characteristics meet the requirements for the high bandwidth suspension in terms of forces and bandwidth. Due to the flat shape of the linear motor, its axial bearings for the actor rod and the ironless secondary part, friction and ripple forces are low. An axial roller bearing is integrated in order to be able to accomodate lateral forces. The actor construction is mechanically robust and tolerates high accelerations and external forces.

In the following the operating principle of the actuator is presented in more detail. A linear motor or linear induction motor is an alternating current (AC) electric motor with an 'unrolled' stator such that, instead of producing a torque, it produces an axial force on the rod. *Linear*

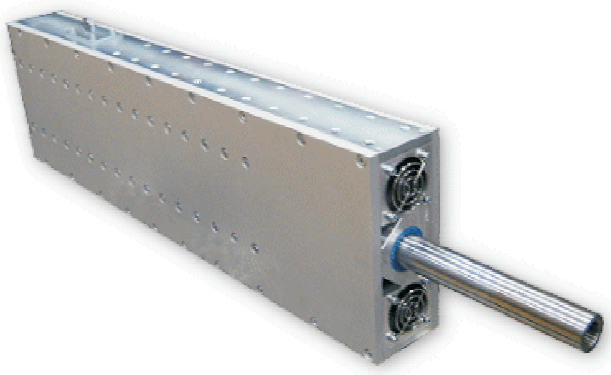

Figure 8: Linear Synchronous Motor

Synchronous Motors (LSMs) generate propulsive forces by running current through a stator, which creates an electro-magnetic field. This electro-magnetic field interacts with a set of permanent magnets to create thrust. The winding (primary part) of the machine is ironless, the secondary part consists of black iron yoke and permanent magnets. The north and south poles are positioned in alternating order to obtain a sinusoidal magnetic flux density characteristic. The symmetrical design and the absence of iron reduce the magnetic attractive force, i.e. an easier mechanical construction and a detent torque, that causes good synchronization in the current control.

The permanent magnets serve as the motor secondary part, equivalent to a rotor in conventional motors enabling linear motion. The movement is regulated by a control system implemented in the inverter. The most common mode of operation is as a Lorentz-type actuator, in which the applied force is linearly proportional to the current and the magnetic field. For the measurement of the rod position, an optical sensor is integrated on the secondary part (see Table 3). Because

Table 3: Technical specifications of the linear synchronous motor

Linear Synchronous Motor	
Specifications	
Max. traverse path	100 mm
Max. velocity	4 m/s
Max. acceleration	90 m/s^2
Continuous force	800 N
Peak force	3200 N
Positioning accuracy	$\pm 1 \mu m$
Direct current link voltage	540 VDC
Dimensions (w/o push rod)	80 x 195 x 680 mm
Push rod diameter	⊘ 30 mm
Push rod mass	5.5 kg
Total mass	33 kg

of the high resistance value, the value of the inductance is low which enables a high bandwidth and very dynamic current/force changes as well as high stiffness with respect to external forces. The motor response to a time-varying input is characterized by an electrical and a mechanical time constant, which are defined by the motor's constructional parameters and are specified as

$$\tau_{el} = 1.73\,\text{ms}\,,$$
$$\tau_{mech} = 3.74\,\text{ms}\,.$$

Furthermore the motor has other physical advantages:

- Low rotor moment of inertia, enabling a fast dynamic behavior,
- low energy losses in the rotor, which provide a good efficiency factor and minimize thermal problems,
- very low standby currents.

In order to reference the position measurement system the rod has to be driven over a reference mark (Figure 9). Thereby, the optical measurement system is activated.

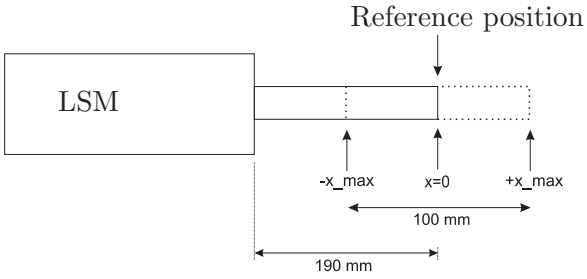

Figure 9: Referencing the position measurement system

3.3 Inverter

The *UD 7000 inverter series* enables the speed control of a three-phase motor by independent control of the output frequency and output voltage [1]. The speed/torque response of the motor remains unchanged due to automatic control of the V/Hz ratio. The *UD 7000 inverters* consist of the two function groups of the power section and inverter control. The core of the inverter control is a 16-bit microcontroller with a non-volatile parameter memory. In conjunction with further circuit components, it controls all necessary inverter functions. In particular, the micro controller generates the pulse width modulated pulses for control of the insulated-gate bipolar transistors (IGBTs). The actuator current is available as measurement signal. More details on the inverter can be found in [1], [2] and [15].

3.4 Internal current and velocity control

The control strategy is based on vector theory, e.g. [17] and [4]. According to [3], the principle of vector control of electrical drives is based on the control of both the magnitude and the phase of each phase current and voltage. For as long as this type of control considers the three phase system as three independent systems the control remains analog and thus present several drawbacks. The most common of these accurate vector controls is *Field Orientated Control (FOC)*, a digital implementation which demonstrates the capability of performing direct torque control, of handling system limitations and of achieving higher power conversion efficiency. This technique consists of controlling the stator currents represented by a vector. This control is based on projections which transform a three phase time and speed dependent system into a two coordinate (d and q coordinates) time-invariant system. These projections lead to a structure similar to that of DC motor control. Field orientated controlled machines need two constants as input references: The torque component (aligned with the q-coordinate) and the flux component (aligned with d-coordinate); a sensor is implemented in the system in order to measure the position of the rod. More details on the velocity control are given in [15].
Figure 10 shows the block diagram of the FO-Control.

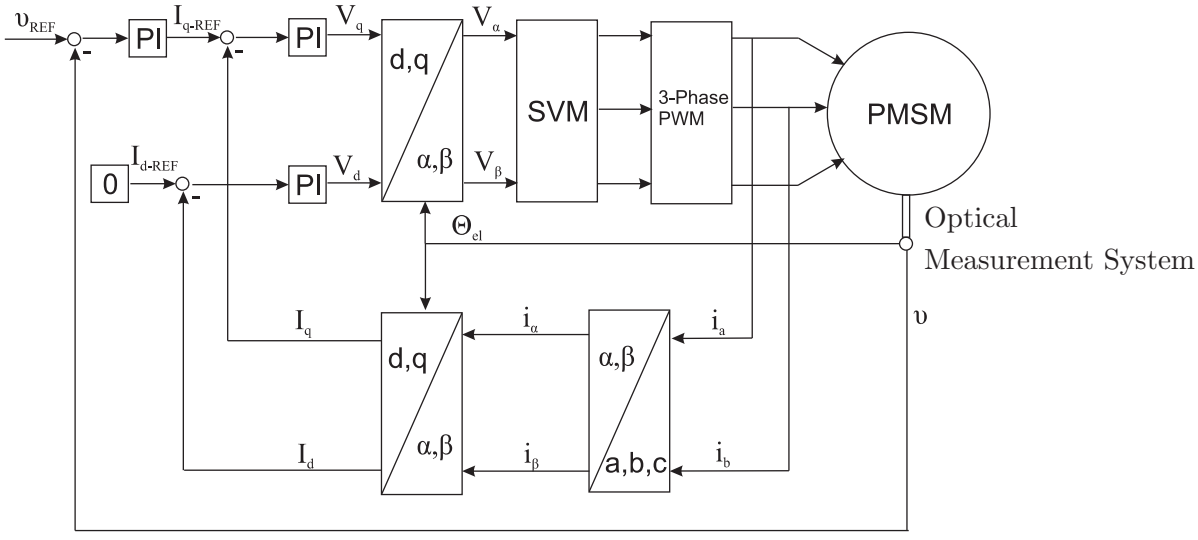

Figure 10: Field oriented control, [15]

As Field Orientated Control is based on projections the control structure handles instantaneous electrical quantities (i_d and i_q). The flux and the velocity control consist of two feedback loops:

One direct-axis component of current loop (i_d) and a cross current loop (i_q). The velocity control loop gives the reference to control the cross current, while the current on the direct-axis is zero. This strategy to control the motor elevates the degree of efficiency of the motor, because its current is perpendicular to the rotor flux. A PI-control strategy is employed (see [1] and Section 4.2) in order to adjust the static control deviation to zero.
By maintaining the amplitude of the rotor flow (ϕ_r) at a fixed value a linear relationship between torque and torque component (i_q) results. Hence, the torque can be expressed as $m_t \propto \phi_r i_q$. The force can be controlled by controlling the torque component of stator current vector.

3.5 Signal processing

The real time signal processing is performed by a *dSpace DS1104* controller board and the software *dSpace Control Desk*. A sampling frequency of 1 kHz is employed. The real time system is connected to a Host-PC, in order to be able to evaluate the signals measured in the process. The sensors are connected to a connector panel. This interface allows the following connections, with the specification summarized in Table 4:

- 8 A/D-Inputs with BNC-connectors (input range ±10 V), 4 of which are multiplexed channels (CP1 ... CP8)
- 8 D/A-Outputs with BNC-connector (CP9 ... CP16)
- one digital I/O-Connector with one 37 pin-connection (CP17)
- one PWM I/O-Connector (CP18)
- two incremental-encoder-interfaces, with 5 V supply voltage (CP19, CP20)
- one serial interface UART RS 232 (CP21)
- one serial interface UART RS 422/RS 485 (CP22)

Table 4: Specifications of the BNC-connectors pin list of the *dSpace Connector Panel CP1104*

dSpace Connector Panel				
	16-bit ADC	12-bit ADC	16-bit DAC	Unit
Theoretical resolution	0.3	4.9	0.3	[mV]
Offset error	± 5	± 5	± 1	[mV]
Gain error	± 0.25	± 0.5	± 0.1	[%]
Signal-to-noise ratio	> 80	> 65	> 80	[dB]

In order to remove noise from the measurement signals, first order lowpass filter circuits with a cutoff frequency of $f_c = 380$ Hz are integrated into the test rig for the analog measurement signals. The resulting signal-to-noise ratios (SNR) and peak-to-peak noise values are given in Table 5. The SNR assume stochastic noise properties and are recorded with disabled actuators. For the determination of the peak-to-peak noise values, the actuators have been enabled. For further reading on SNR and quantification of signal quality [16], [14] [5] are recommended.

Table 5: Signal-to-noise and peak-to-peak noise ratios of the measurement signals

Measurement Signal	SN-ratio	Peak-to peak noise ratio
Chassis acc.	70 dB	40 mV
Wheel acc.	65 dB	40 mV
Wheel load	75 dB	50 mV
Actuator current	-	100 mV

4 Modeling and identification of the test rig dynamics

In this Section, the modeling and identification of the test rig is presented. The aim is a model that accurately matches the test rig's dynamic behavior in the frequency range $0 - 25\,\text{Hz}$. A nonlinear model including actuator dynamics is desired for simulation purposes and a linear model will be used for controller design. This Section describes the actuator modeling and the main nonlinearities of the test rig, the modeling of friction effects, the parameter identification procedure and the performance evaluation of the nonlinear and the linear test rig model.

It is noted that the focus of this Section is on the experimental identification methods and the model structure. Due to continuous modifications of the test rig, not all identified characteristiccs resemble the current test rig status. These characteristics are marked and the current parameter set is given in Section 4.6.

4.1 Linear quarter-vehicle model

If only the primary vertical dynamical degree of freedom, the translatory movement of the wheel and the chassis mass, is considered, a full car model can be simplified to the well known quarter-vehicle model [12]. This implies the assumption of symmetry for the full-vehicle model and the negligence of coupling effects. Figure 11 shows the quarter-vehicle models of a passive suspension system (left) and a high bandwidth active suspension system (right, with control force $F(t)$) that is considered for the active suspension on the test rig. Although the influence of tire damping for cars is usually low in the considered low frequency range [12], the tire damping is included in the considered quarter-vehicle model because the tire dynamics are identified including its (small) damping (see Section 4.3).

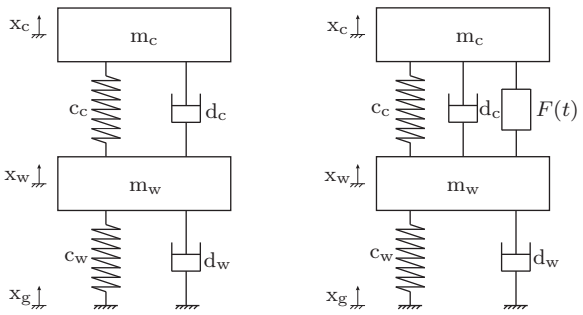

Figure 11: Quarter-vehicle suspension models: Passive suspension (left) and high bandwidth active suspension (right)

The equations of motions of the active system (Figure 11 right) including passive damping are derived with $F(t)$ denoting the actuator force and assuming linear component characteristics

(tire, primary spring and damper) as follows

$$m_c\ddot{x}_c = -c_c\,(x_c - x_w) - d_c\,(\dot{x}_c - \dot{x}_w) + F(t) \tag{2}$$
$$m_w\ddot{x}_w = c_c\,(x_c - x_w) + d_c\,(\dot{x}_c - \dot{x}_w) - c_w\,(x_w - x_g) - d_w\,(\dot{x}_w - \dot{x}_g) - F(t)\,. \tag{3}$$

The state-vector $\mathbf{x}$, the control input u and the disturbance input u_d are introduced as

$$\mathbf{x} = \begin{bmatrix} x_c - x_w \\ \dot{x}_c \\ x_w - x_g \\ \dot{x}_w \end{bmatrix} \quad , \quad u = F(t) \quad , \quad u_d = \dot{x}_g\,. \tag{4}$$

In the output vector y the variables, which are of primary interest for suspension control, are summarized. Besides the minimization of the vertical body acceleration $\ddot{x}_c$, the dynamic wheel load

$$F_{dyn} = d_w(\dot{x}_g - \dot{x}_w) + c_w(x_g - x_w) \tag{5}$$

has to be bound in order to guarantee ride safety and the suspension deflection $x_c - x_w$ must be kept within the constructionally conditioned limits. Hence, the output vector is defined as follows

$$\mathbf{y} = \begin{bmatrix} \ddot{x}_c \\ F_{dyn} \\ x_c - x_w \end{bmatrix}. \tag{6}$$

The quarter-vehicle model can be expressed as a state space model of the form

$$\dot{\mathbf{x}} = \mathbf{A}\mathbf{x} + \mathbf{B}u + \mathbf{E}u_d \quad , \tag{7}$$
$$\mathbf{y} = \mathbf{C}\mathbf{x} + \mathbf{D}u + \mathbf{F}u_d \tag{8}$$

as

$$\begin{bmatrix} \dot{x}_1 \\ \dot{x}_2 \\ \dot{x}_3 \\ \dot{x}_4 \end{bmatrix} = \begin{bmatrix} 0 & 1 & 0 & -1 \\ -\frac{c_c}{m_c} & -\frac{d_c}{m_c} & 0 & \frac{d_c}{m_c} \\ 0 & 0 & 0 & 1 \\ \frac{c_c}{m_w} & \frac{d_c}{m_w} & -\frac{c_w}{m_w} & -\frac{d_c+d_w}{m_w} \end{bmatrix} \begin{bmatrix} x_1 \\ x_2 \\ x_3 \\ x_4 \end{bmatrix} + \begin{bmatrix} 0 \\ \frac{1}{m_c} \\ 0 \\ -\frac{1}{m_w} \end{bmatrix} u + \begin{bmatrix} 0 \\ 0 \\ -1 \\ 1 \end{bmatrix} u_d \quad ,$$

$$\begin{bmatrix} \ddot{z}_c \\ F_{dyn} \\ x_c - x_w \end{bmatrix} = \begin{bmatrix} -\frac{c_c}{m_c} & -\frac{d_c}{m_c} & 0 & \frac{d_c}{m_c} \\ 0 & 0 & -c_w & -d_w \\ 1 & 0 & 0 & 0 \end{bmatrix} \mathbf{x} + \begin{bmatrix} \frac{1}{m_c} \\ 0 \\ 0 \end{bmatrix} u + \begin{bmatrix} 0 \\ d_w \\ 0 \end{bmatrix} u_d \quad . \tag{9}$$

Note that the quarter-vehicle model of the passive suspension results if the control force vanishes ($u(t) = 0$).

This simple linear quarter-vehicle model has several advantages: Due to its simple structure and low dynamic order it offers an intuitive understanding of the vertical dynamic behavior. Moreover, it offers a good basis for controller design. Nevertheless, in order to accurately model the quadricycle suspension, the suspension nonlinearities and the actuator dynamics have to be determined by means of system identification first.

4.2 Actuator model

The PI-controller setting of the inverter has been optimized to increase the actuator bandwidth. The bode diagram of the actuator (Figure 12) shows a bandwidth (−3 dB cutoff frequency) of

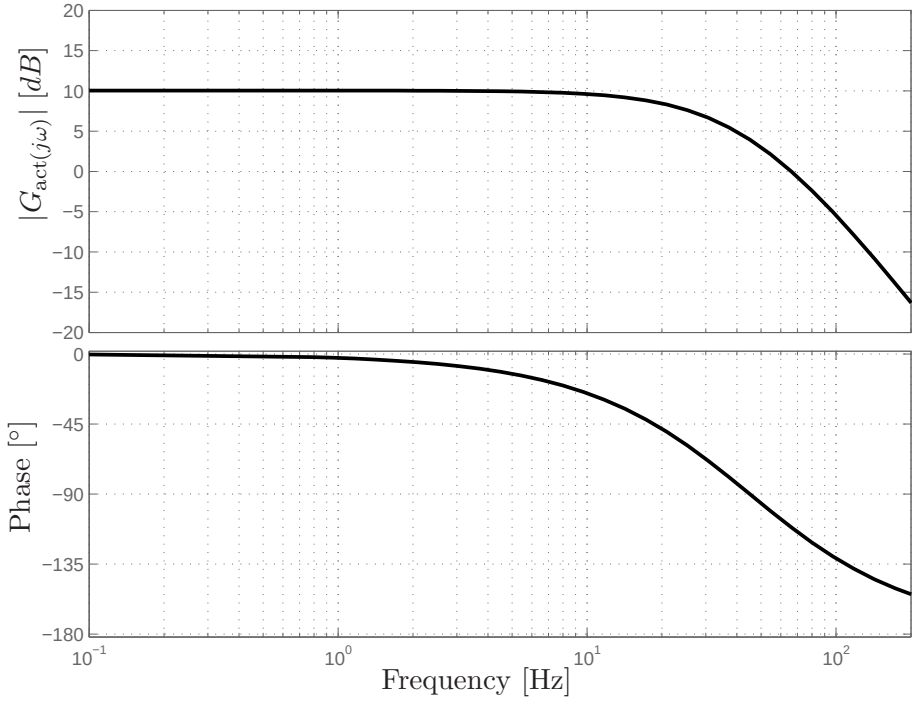

Figure 12: Bode diagram for the actuator model

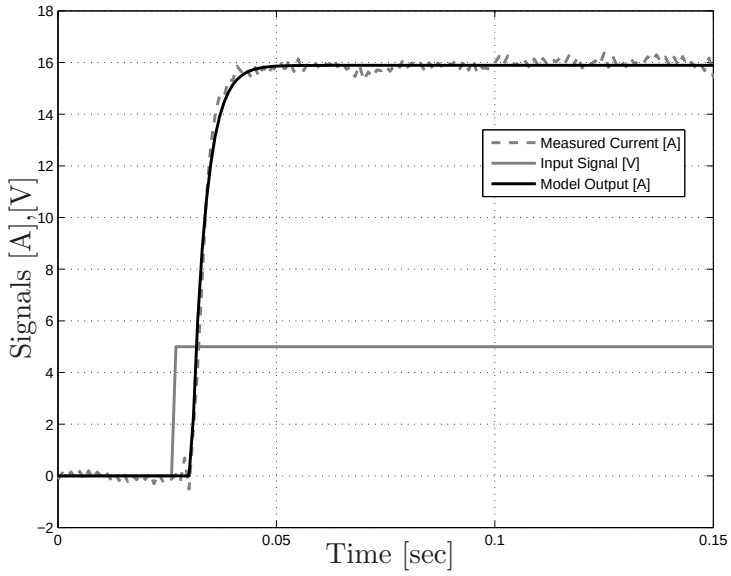

Figure 13: Response of the actuator force to a 5 V step input

approx. $\omega_c = 2\pi \cdot 28.6$ Hz. The response of the model to a 5V-step input of the control signal $u_v(t)$ is shown in Figure 13.

The actuator current's dynamic behavior can be modeled using a first order model. The time delay of $T_d = 4$ ms has been included in the model using a first order Padé-Approximation. The

resulting model is

$$\begin{bmatrix} \dot{v}_1 \\ \dot{v}_2 \end{bmatrix} = \begin{bmatrix} -320.4019 & 0 \\ 250 & -250 \end{bmatrix} \begin{bmatrix} v_1 \\ v_2 \end{bmatrix} + \begin{bmatrix} 1.2131 \\ 0 \end{bmatrix} u_v \tag{10}$$

$$i_{act} = \begin{bmatrix} 0 & 839.4076 \end{bmatrix} \begin{bmatrix} v_1 \\ v_2 \end{bmatrix} \tag{11}$$

with v_1 and v_2 being the actuator states and i_{act} being the actuator current proportional to the actuator force ($1\,\mathrm{A} \sim 1\,\mathrm{kN}$).

4.3 Test rig identification: A nonlinear gray-box model approach

The quarter-vehicle test rig is used to record I/O-data of the suspension in order to identify a nonlinear model of the suspension system. This is done in three steps, which are presented in detail in the following Sections:

1. The spring and damping characteristics of the primary spring and damper as well as the tire are identified individually on separate setups of the test rig.
2. These nonlinear characteristics are embedded in a nonlinear model structure including a friction model. The remaining parameters of this structure are optimized using least square parameter identification routines.
3. The parametrized nonlinear model is validated using measurement data recorded with the complete test rig being in operation.

For the identification of each component characteristic, an appropriate design of experiments in terms of hardware setting and excitation signals has been conducted. The stiffness and damping characteristics of the components are identified in the assembled state of the components in the test rig. This has the advantage that all kinematic effects causing nonlinearities are included in the characteristics of the spring and the damper since the component of their forces parallel to the suspension is a nonlinear function of the wheel's vertical position because of the kinematics of the double wishbone struts.

4.3.1 Identification of the primary spring and damper For the identification of the primary spring's stiffness characteristic the tire has been removed from the test rig and the sprung mass m_c representing the chassis mass has been clamped. The wheel carrier is moved vertically quasi-statically ($\dot{x}_w = 2\frac{\mathrm{mm}}{\mathrm{sec}}$) by the linear motor and the force as well as the position of the wheel carrier are measured. The stiffness measurement is shown in Figure 14 and a hysteresis curve resulting from friction effects can be seen. From the hysteresis curve a static friction force of approx. $\pm 94\,\mathrm{N}$ can be determined. Note that in the current test rig status a different spring with a linear characteristic is used (see Section 4.6).

In order to identify the damper characteristic the same test-setup as for the spring identification has been used but the damper has been excited dynamically using sinusoidal chirp signals (within the frequency range $0 - 5\,\mathrm{Hz}$). The analysis of measurement data has shown that a steeper damper characteristic occurs for rebound than for compression (see Figure 15). This is conform with automotive dampers and results from the construction of the hydraulic dampers [12].

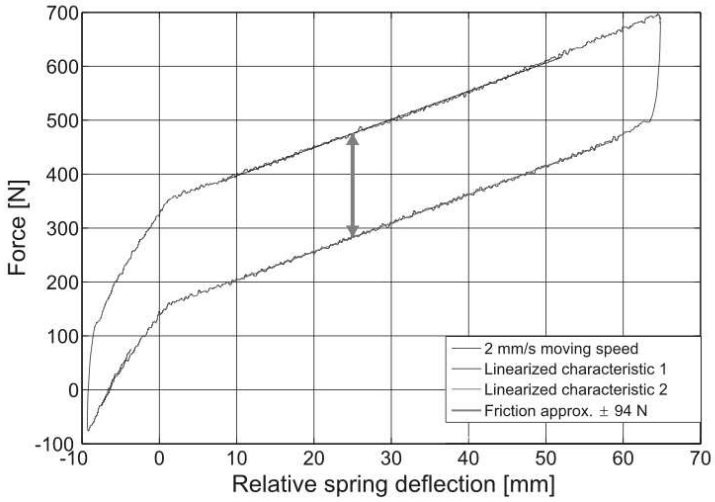

Figure 14: Identification result for spring characteristic (Status: 01/2009)

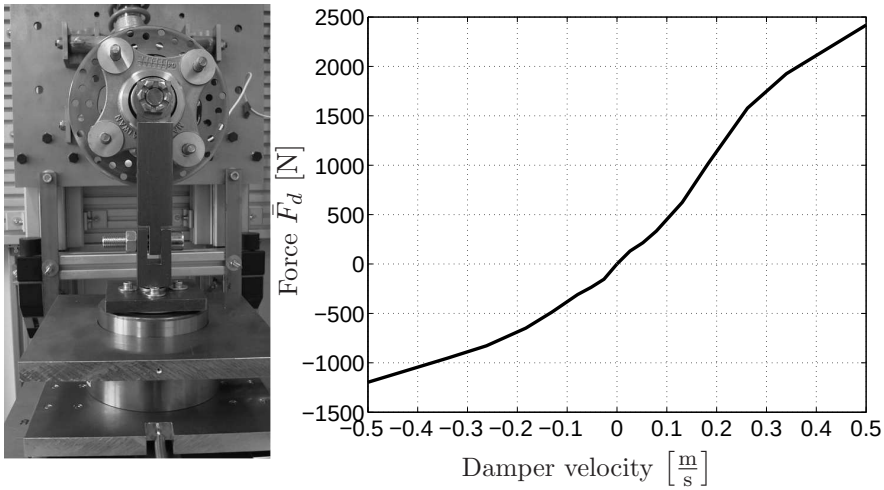

Figure 15: Experimental setup for the damper identification and nonlinear characteristic the damper

4.3.2 Tire characteristic For the determination of the tire properties, the primary spring has been replaced by a stiff steel rod and the chassis mass has been clamped again. Therefore, the only relevant elasticity in the setup is the tire. Its spring characteristic has been measured applying a quasi-static deflection by the linear motor with a tire pressure of 1.4 bar at room temperature.

The tire has a quadratic characteristic (Figure 16) which can be approximated well by a second order polynomial. For a linear model, the tire characteristic can be linearized at the operating point characterized by the static wheel load. The linearized spring rate of the tire is $152186\frac{\mathrm{N}}{\mathrm{m}}$. The tire damping has been identified by parameter optimization ($d_w = 50\,\frac{\mathrm{Ns}}{\mathrm{m}}$) because the lower actuator could not provide a sufficiently dynamic excitation signal. The comparably small damping coefficient of the tire is coherent with the literature stating that the tire damping can be neglected for a quarter-vehicle model [12].

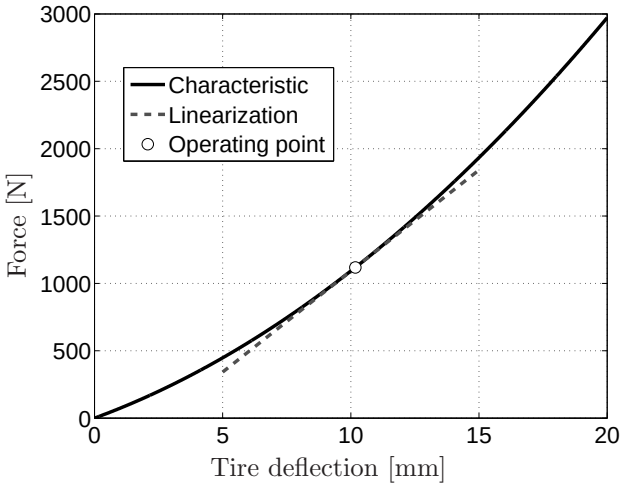

Figure 16: Nonlinear force-deflection characteristic of the tire

4.3.3 Friction effects Coulomb friction forces (see e.g. [13]) in the suspension ($F_{f,1}$) and in the vertical linear guides of the chassis mass ($F_{f,2}$) are taken account for the modeling (see also [7]). The Coulomb friction forces are approximated by tanh-functions for smooth zero crossings (see e.g. [9]) and the resulting friction model (Figure 17) is

$$F_{f,i} = \hat{F}_{f,i} \tanh(\Delta v_i k_{f,i}) \tag{12}$$

with $\Delta v_1 = \dot{x}_c$, $\Delta v_2 = \dot{x}_c - \dot{x}_w$ and the scaling factors $k_{f,1} = k_{f,2}$. The numerical values are given in Section 4.6 in Table 10.

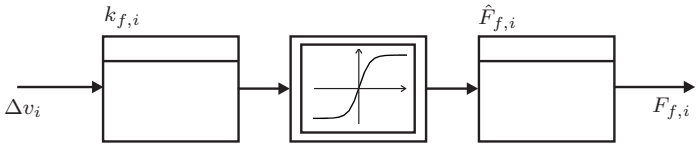

Figure 17: Friction model

4.3.4 Suspension kinematics The integration of the suspension kinematics in an analytical nonlinear model has been presented by the authors in [8]. Because of the design of experiments presented in this report they are already included in the nonlinear characteristic of the damper and the spring constant of the primary spring. However, they are needed e.g. for observer design to estimate the damper velocity from the measured acceleration signals (see [8], [7]).

The nonlinearities caused by the kinematics of the suspension system can be considered using a transmission factor $i_c = \frac{\Delta \dot{x}_{el}}{\dot{x}_c - \dot{x}_w}$ (with $\Delta \dot{x}_{el}$ being the relative velocity of the suspension strut in the direction of the element's center line). The factor transforms the forces and kinematic relations at the elements (spring force $\bar{F}_{cc} = \bar{c}_c \Delta x_{el}$, damper force $\bar{F}_d$) to the corresponding quantities of the quarter-vehicle model (Figure 11), i.e. the forces acting on the center of gravity of the wheel. According to [11] for the primary spring stiffness results

$$c_c = i_c^2 \bar{c}_c + \bar{F}_{cc} \frac{di_c}{d(x_c - x_w)} \,. \tag{13}$$

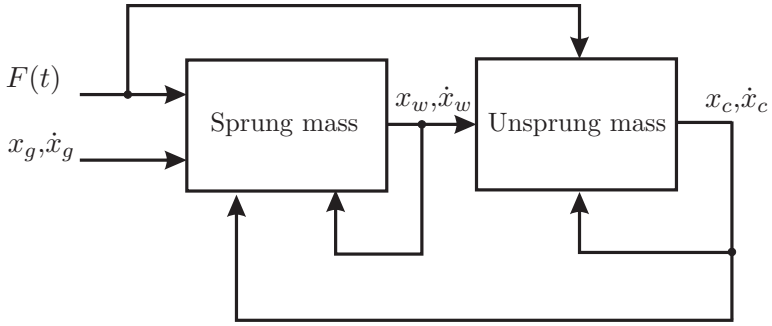

Figure 18: Nonlinear quarter-vehicle model

The second term in (13) can be neglected in the model because it has been identified to be small. This identification has been performed using two wire rope actuated position transducers (WRAPT): One has been attached to the spring (compare Figure 2) and the second one is attached to the center of the wheel and the chassis mass, thus measuring the displacement in the plane of the wheel as described in the quarter-vehicle model. Due to the concentric configuration of the suspension strut, the transmission ratio is the same for the spring and the damper, such that $i_c = i_d = i = 0.392$ holds and for the damper force results $F_d = i\bar{F}_d$.

4.4 Nonlinear model structure

In the following block-diagrams illustrate the structure of the nonlinear gray-box model of the quarter-vehicle test rig. The nonlinear identified characteristics presented in previous Sections are illustrated schematically in the subsystems.

Figure 18 depicts the basic structure consisting of the connected sprung and unsprung masses of the suspension system. The inputs of the system are the excitation (x_g,$\dot{x}_g$) and the actuator force $F(t)$. The output signals are the positions and velocities of the masses forming the state vector of the basic quarter-vehicle model. Figure 19 illustrates the model of the unsprung mass movement that interacts with the sprung mass (Figure 20). The subsystems for the tire damping (Figure 21) also contains a Coloumb friction term and the nonlinear tire stiffness is depicted in Figure 22. Coulomb friction is also added to the measured damper characteristic (Figure 23).

A linear spring stiffness c_c resulting in the spring force

$$F_c = c_c(x_c - x_w) \tag{14}$$

is a very good approximation of the measured spring characteristic (Figure 14) in the operating range of the test rig, which is determined by the actuator's maximum stroke ($\pm 5\,\mathrm{cm}$). The roll friction force of the chassis mass is modeled according to (12).

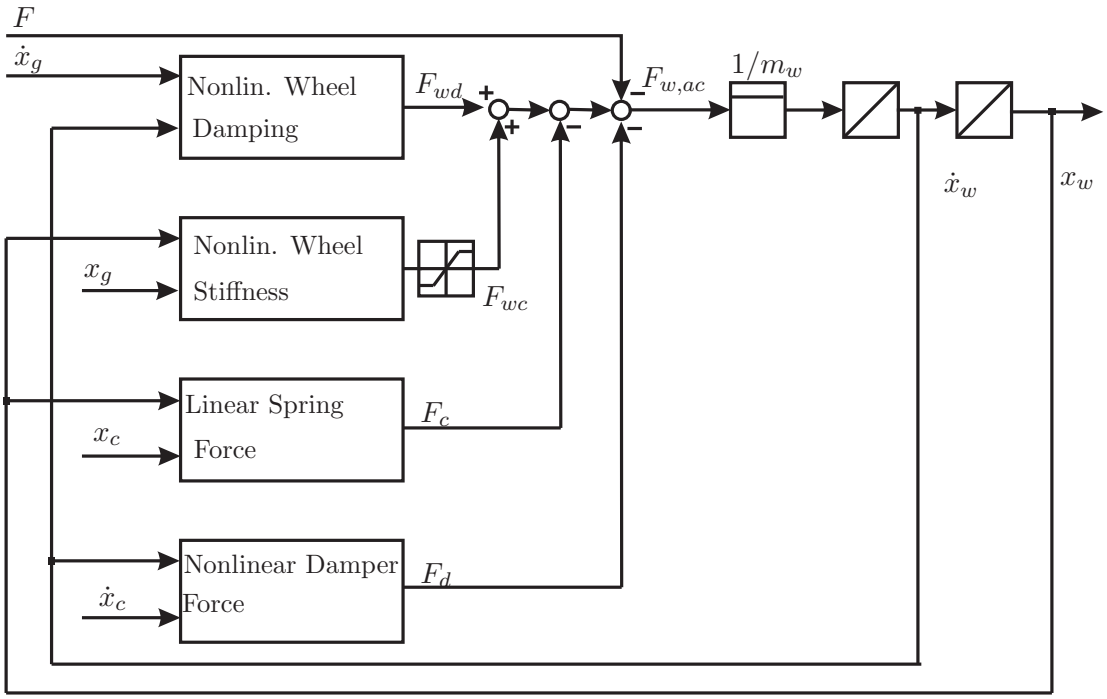

Figure 19: Nonlinear unsprung mass model

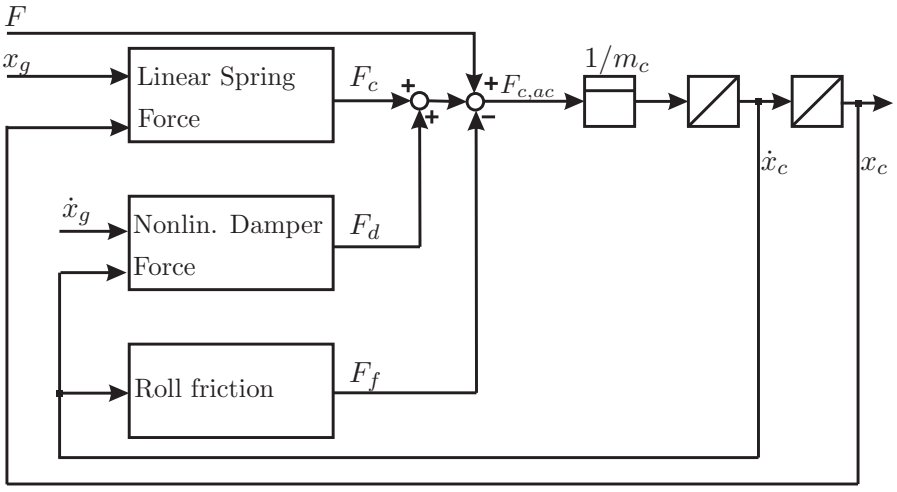

Figure 20: Nonlinear sprung mass model

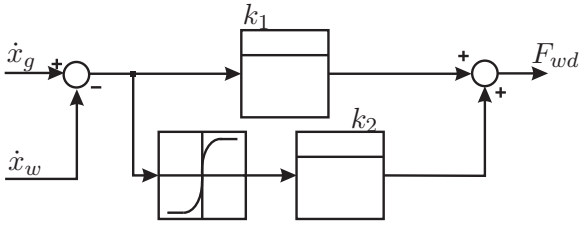

Figure 21: Unsprung mass: Nonlinear tire damping

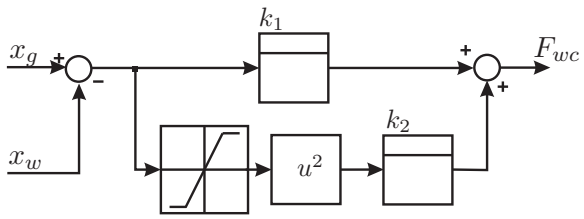

Figure 22: Unsprung mass: Nonlinear tire stiffness

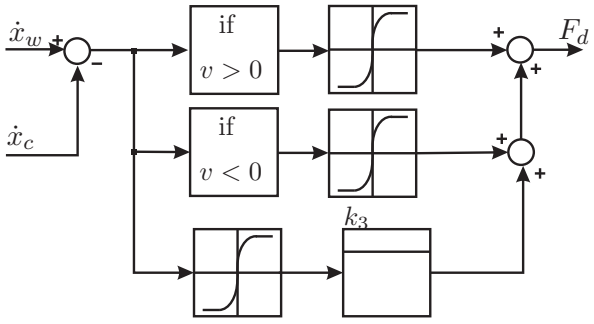

Figure 23: Nonlinear damper force

4.5 Parameter identification

In total, the nonlinear model has a variety of 13 parameters to be identified. The tire dynamics are described by a linear and a quadratic stiffness rate, a linear damping coefficient and Coloumb friction between tire and the base plate described by a velocity scaling factor for the tanh-function (compare (12)) and the friction force (see Section 4.4). The force between chassis and wheel constitutes from the linear spring stiffness, the nonlinear damping characteristic in rebound and compression, a Coloumb friction described by the scaling factor $k_{f,1}$ in (12) and the corresponding friction force $\hat{F}_{f,1}$. As the chassis mass motion is guided vertically (as shown in Figure 2), the friction between the chassis and the inertial system must be simulated by another Coulomb friction force model with the parameters $k_{f,2}$ and $\hat{F}_{f,2}$. The most important influence on the dynamics results from the total mass of the quarter-vehicle and its distribution into sprung and unsprung mass.

To identify the parameter set that leads to the best simulation results of the real quarter-vehicle dynamics, a gradient-based optimization algorithm is used. The relevant variables for the quarter-vehicle dynamics are the dynamic wheel force and the acceleration of chassis and wheel. Therefore, the cost function

$$f(x) = 1 - \overline{f}(x) = 1 - (0.4\Phi_{\ddot{z}_c} + 0.4\Phi_{F_{dyn}} + 0.2\Phi_{\ddot{z}_w}) \tag{15}$$

constitutes of the sum of the weighted performance indices of these signals. Where the performance index is defined with the root-mean-square values (rms) of the signal ($\|z\|_{\text{rms}}$) and the simulation error ($\|e\|_{\text{rms}}$) as

$$\Phi = 1 - \frac{\|e\|_{\text{rms}}}{\|z\|_{\text{rms}}}\,. \tag{16}$$

To handle the high number of optimization parameters their uncertainty and the models' sensitivity to their variation has to be considered. This leads to the following approach: The

variation of parameters with a small uncertainty is strictly constrained to a narrow range and the number of optimized parameters is increased after every optimization run. The parameter with least uncertainty is the total mass, because every mounted part of the test rig has been precisely weighted. Consequently the total mass is fixed, while its distribution into sprung and unsprung mass is the only degree of freedom regarding the mass parameters. The uncertainty is determined by the mass of the suspension parts (double wishbone, damper, spring) as these masses cannot be clearly allocated to the sprung or unsprung mass. Therefore, the constraints result from assigning the suspension mass either completely to the chassis (sprung) or the wheel (unsprung) mass. The mass distribution, the spring rate and the damping rates for compression and rebound have the most significant influence on the vehicle dynamics and are optimized in the first run. In the second run the tire dynamics (2 stiffness parameters and the tire damping) as well as the remaining 6 friction parameters are varied by the algorithm, but the parameters of the first run are bounded to a $\pm 5\%$ variation compared to the resulting values of the first run.

The optimization is based on the *MATLAB* function *fmincon* [10], which searches for the minimum of a given cost function using a gradient-based algorithm and considers given constraints. The optimization procedure varies the values of the parameter vector $\vec{x}$, which includes the n adjustable parameters of the quarter-car model, performs a simulation run for each case and determines numerically the n-dimensional gradient

$$grad\ f(\vec{x}_k) = \frac{\partial f}{\partial \vec{x}}|_{\vec{x}_k} = \nabla f(\vec{x}_k) \tag{17}$$

of the cost function $f(\vec{x})$ (see (15)) at the parameter vector $\vec{x}_k$ of the optimization step k. Accordingly the parameter variation

$$\vec{x}_{k+1} = \vec{x}_k - \nabla f(\vec{x}_k) \cdot \Delta x \tag{18}$$

with the step size Δx in the negated direction of the gradient, as this is the direction of the steepest descent. At this point the determination of the gradient restarts. Since the gradient at the minimum of a continuously differentiable function is the zero vector, the Euclidian norm of the gradient is used as the termination condition. If the norm drops below a certain value, the algorithm will be aborted. Since this does not guarantee a global minimum, the optimization function is primarily initialized with large step sizes and early termination conditions to find the region of the global minimum. Then these values are reduced iteratively. As start vector the empirical identification results are used and the assumption that they are close to the global minimum increases the probability that the routine converges towards the global minimum.

To ensure good simulation results with alternating road profiles, two simulations with different measured road profiles are run and the optimization routine uses the mean value of the cost functions of both simulation results.

4.6 Model comparison and validation

Table 6 summarizes the performance indices Φ_i for the signals, which can be compared to the measured reference signals of the sensors. The optimized parameter set for the nonlinear model is given in Table 7. For the determination of the natural frequency and the damping ratios, the damper has been linearized in the operating range $\pm 0.4\,\frac{\mathrm{m}}{\mathrm{s}}$ (in the quarter-vehicle model description) and the tire force deflection charateristic has been linearized in the operating point (see Figure 16). Note that for the parameter set given in Table 7, a characteristic of the damper has been used that has been provided by its manufacturer.

Table 6: Performance indices of the nonlinear simulation for excitation by typical road profile

Performance index Φ of simulation for	Optimized parameters	Measured parameters
Chassis position x_c	0.883	0.841
Chassis acceleration $\ddot{x}_c$	0.844	0.808
Dyn. wheel force F_{dyn}	0.793	0.795
Wheel acceleration $\ddot{x}_w$	0.608	0.645

Table 7: Optimized parameters of the nonlinear quarter-car model

Nonlinear model parameters	Optimized	Measured	Unit
Linear tire stiffness	138820	149693	N/m
Quadratic tire stiffness	4075400	3940000	N/m
Tire damping	37.9	50	Ns/m
Chassis spring stiffness	7980	8250	N/m
Sprung mass	91.23	89.56	kg
Unsprung mass	22.25	23.92	kg
Total mass	113.48	113.48	kg
Friction spring/damper	105	100	N
Friction chassis guides	23.8	10	N
Friction tire	62.8	60	N
Undamped natural frequency chassis	1.49	1.51	Hz
Damping ratio chassis	0.47	0.443	-
Undamped natural frequency wheel	12.92	12.59	Hz
Damping ratio wheel	0.212	0.196	-

All friction scaling factors are $k_{f,i} = 125$ and the transmission ration is $i = 0.392$.

Table 6 shows good performance index values for the chassis dynamics and the wheel force, while the estimation of the wheel acceleration has the smallest performance index value. By optimizing the parameter set the simulation of the chassis dynamics could be improved with an almost unchanged index for the wheel force. Due to the composition of the cost function, the performance of the simulation of the wheel acceleration shows a small decrease. Figure 24 compares measured and simulated signals and it can be seen that the model matches the measurement signals well. The chassis position shows only low-frequency deviations, while the other signals have primarily high-frequency errors.

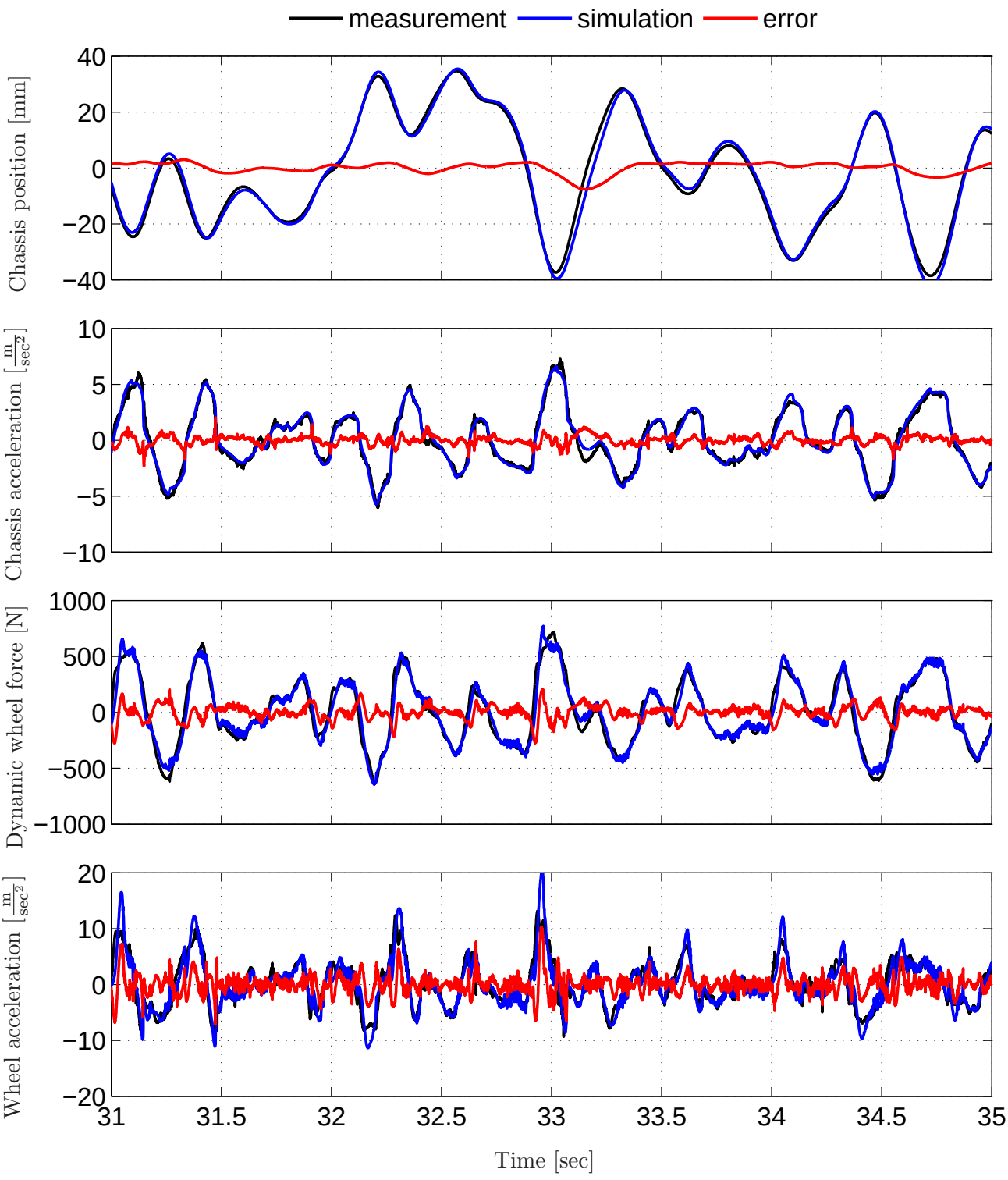

Figure 24: Comparison of measurement and simulation result with the nonlinear model using the optimized parameter set

The linear model is constructed from the linearization of the tire characteristic, the omission of the friction models and a linearized damping ratio calculated from the mean of the optimized damping ratios for rebound and compression. A significant improvement of the simulation performance of the linear model has been achieved (see Table 8) by another optimization run for the parameters after these linearization operations (compare Table 9).

The performance indices for all signals have been considerably improved, the errors due to the missing nonlinear effects have been partially equalized by optimization based adjustments of the parameters of the linear model. The comparison of simulated and measured signals shows overall an acceptable reproduction but in detail the simulation results apparently show a lower performance than those resulting from the nonlinear model.

Table 8: Performance indices of the linear simulation for excitation by a typical road profile

Performance index Φ of simulation for	Optimized parameters	Measured parameters
Chassis position z_c	0.785	0.608
Chassis acceleration $\ddot{z}_c$	0.737	0.501
Dyn. wheel force F_{dyn}	0.725	0.5692
Wheel acceleration $\ddot{z}_w$	0.614	0.520

Table 9: Optimized parameters of the linear quarter-car model

Linear Model Parameters	Optimized	Measured	Unit
Tire stiffness	178000	149693	N/m
Tire damping	123	100	Ns/m
Chassis spring stiffness	6952	8250	N/m
Chassis compression damping	794	521	Ns/m
Chassis rebound damping	1510	994	Ns/m
Chassis linear damping	1152	758	Ns/m
Sprung mass	91.23	89.56	kg
Unsprung mass	22.25	23.92	kg
Total mass	113.48	113.48	kg
Undamped natural frequency chassis	1.39	1.51	Hz
Damping ratio chassis	0.723	0.447	-
Undamped natural frequency wheel	14.24	12.59	Hz
Damping ratio wheel	0.284	0.198	-

The current parameters for the nonlinear model (test rig status 05/2010) are given in Table 10. They deviate from the parameters given in Table 7 due to minor modifications of the test rig hardware.

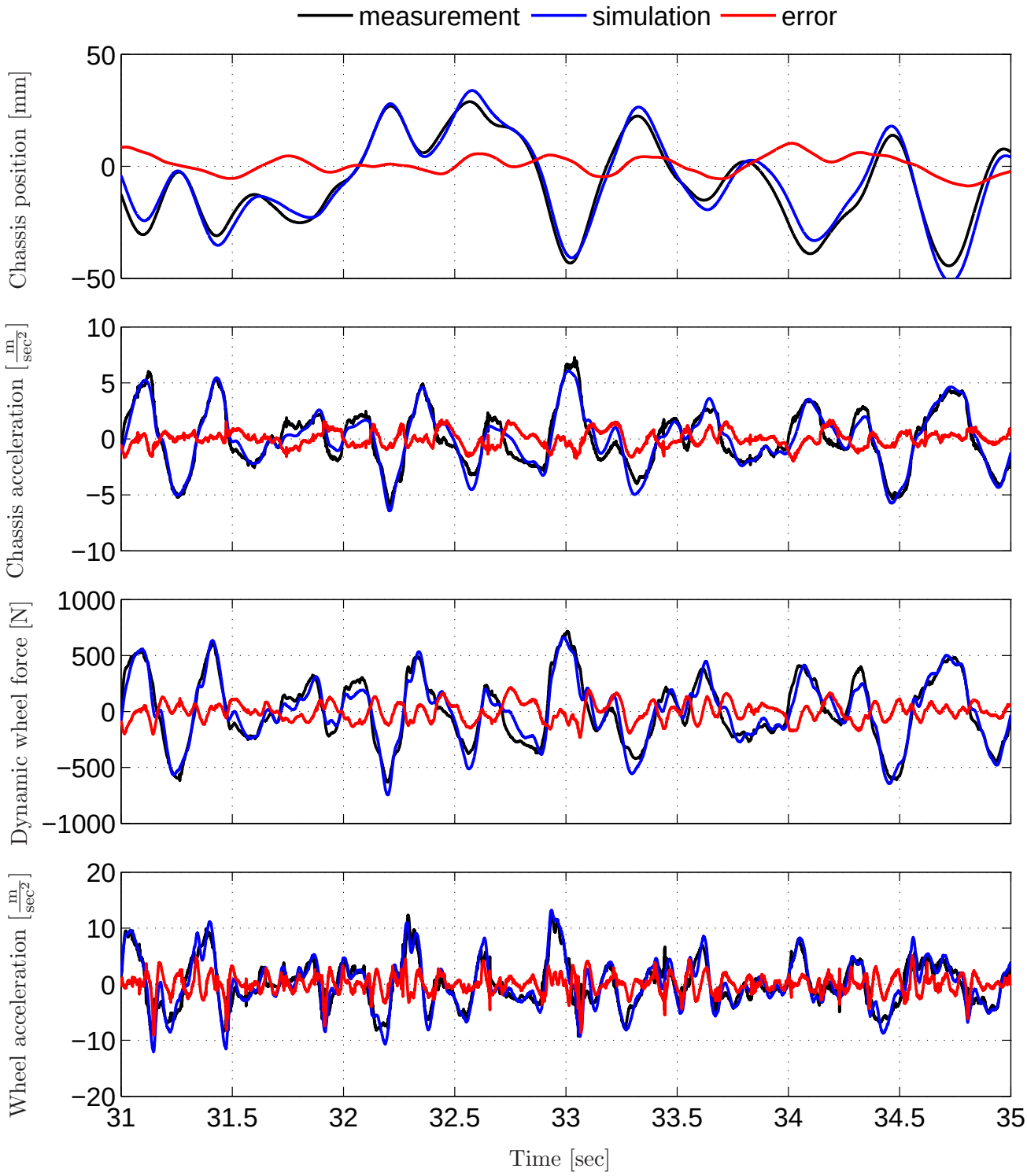

Figure 25: Comparison of measurement and simulation result with the linear model using the optimized parameter set

Table 10: Optimized parameters of the nonlinear quarter-car model (status 05/2010)

Nonlinear model parameter	Value	Unit
Linear tire stiffness	152140	N/m
Quadratic tire stiffness	4075400	N/m
Tire damping	50	Ns/m
Chassis spring stiffness $c_c = i^{-2}\bar{c}_c$	8400	N/m
Transmission ratio i	0.392	-
Sprung mass	94.38	kg
Unsprung mass	23.92	kg
Total mass	118.3	kg
Friction spring/damper $F_{f,1}$	115	N
Friction scaling $k_{f,1}$	125	-
Friction chassis guides $F_{f,2}$	20	N
Friction scaling $k_{f,2}$	125	-
Friction tire	0	N
Undamped natural frequency chassis	1.5	Hz
Damping ratio chassis	0.397	-
Undamped natural frequency wheel	12.7	Hz
Damping ratio wheel	0.18	-

5 Conclusion

The design of a quarter-vehicle test rig as well as its modeling has been presented. With the electrical linear motor a high bandwidth active suspension system with a control bandwidth of more than 28 Hz has been realized, which fulfills all requirements of the authors. The active suspension system is equipped with a sensor configuration comparable to modern production-vehicles and can be excited by real measured road profile signals. Thus, a realistic framework for experimental validation of suspension controllers is guaranteed. The nonlinear model of the test rig has been obtained by system identification techniques using a physically motivated gray-box model structure and gradient based parameter optimization. The model matches the dynamic behavior of the test rig well and can be used for controller design and simulation.

Acknowledgements

The authors would like to thank Thomas Huber for his extensive collaboration in the test rig planning and for realizing its construction. Moreover, the authors would like to thank all students, who worked on the test rig and contributed to its current status. Finally, the authors' thanks go to Andreas Unger for reviewing this report.

References

[1] BERGES electronic GmbH. *Betriebsanleitung Teil 1 (1.5-55, Software A19.07)*, In: http://www.bergeselectronic.com edition, zugegriffen am: 29.11.2007.

[2] BERGES electronic GmbH. *Parameterbeschreibung Teil 2*, In: http://www.bergeselectronic.com edition, zugegriffen am: 29.11.2007.

[3] Lucio Bonometti. *Convertitori di potenza e servomotori brushless*. UTET, Torino, -. Seconda edizione riveduta ed ampliata.

[4] S. Brückl. Regelung von Synchron-Linearmotoren für hochgenaue Vorschubantriebe bei Werkzeugmaschinen. Dissertation bei der TU München - Lehrstuhl für Feingerätebau und Mikrotechnik, 1999-2000.

[5] dSpace GmbH. *sSpace DS1103 PPC Controller Board - Hardware Installation and Configuration*, Release 6.4 edition, 2009.

[6] B. Heißing. *Fahrwerkhandbuch*. Vieweg Verlag, Wiesbaden, 2007.

[7] G. Koch, T. Kloiber, and B. Lohmann. Nonlinear and filter based estimation for vehicle suspension control. In *Submitted to the 49th IEEE Conference on Decision and Control*, 2010.

[8] G. Koch, T. Kloiber, E. Pellegrini, and B. Lohmann. A nonlinear estimator concept for active vehicle suspension control. In *Proc. of the 2010 American Control Conference*, 2010.

[9] U. Kramer. *Kraftfahrzeugführung: Modelle, Simulation und Regelung*. Hanser Verlag, 2007.

[10] The Mathworks. *MATLAB Optimization Toolbox 5 - User's Guide*, 2010.

[11] W. Matschinsky. *Radführungen der Straßenfahrzeuge - Kinematik, Elasto-Kinematik und Konstruktion*. Springer, 2007.

[12] M. Mitschke and H. Wallentowitz. *Dynamik der Kraftfahrzeuge*. Springer, Berlin, 2004.

[13] H. Olsson, K.J. Åström, C. C. de Wit, M. Gäfvert, and Lischinsky. P. Friction models and friction compensation. *European Journal of Control*, 4(3):176 – 195, 1998.

[14] H. W. Ott. *Electromagnetic Compatibility Engineering*. John Wiley & Sons, 2009.

[15] Enrico Pellegrini. Modellierung, Ansteuerung und Regelung eines hochdynamischen Linearmotors zur aktiven Schwingungsdämpfung eines Kfz-Fahrwerks. Diplomarbeit am Lehrstuhl für Regelungstechnik - TUM, 2007-2008. Betreuer: Dipl.-Ing. G. Koch.

[16] W.-D. Schmidt. *Sensorschaltungstechnik*. Vogel Industrie Medien, 3 edition, 2007.

[17] Dierk Schröder. *Elektrische Antriebe - Regelungen von Antriebsysteme*. Springer-Verlag, 2001. 2. Auflage.